Patterned Radial GaAs Nanopillar Solar Cells

Giacomo Mariani,*,[†] Ping-Show Wong,[†] Aaron M. Katzenmeyer,[§] Francois Léonard,[§] Joshua Shapiro,[†] and Diana L. Huffaker[†,‡]

[†]Electrical Engineering Department and [‡]California NanoSystems Institute, University of California at Los Angeles, Los Angeles, California 90095, United States

[§]Sandia National Laboratories, Livermore, California 94551, United States

ABSTRACT: Photovoltaic devices using GaAs nanopillar radial p−n junctions are demonstrated by means of catalyst-free selective-area metal−organic chemical vapor deposition. Dense, large-area, lithographically defined vertical arrays of nanowires with uniform spacing and dimensions allow for power conversion efficiencies for this material system of 2.54% (AM 1.5 G) and high rectification ratio of 213 (at ±1 V). The absence of metal catalyst contamination results in leakage currents of ∼236 nA at −1 V. High-resolution scanning photocurrent microscopy measurements reveal the independent functioning of each nanowire in the array with an individual peak photocurrent of ∼1 nA at 544 nm. External quantum efficiency shows that the photocarrier extraction highly depends on the degenerately doped transparent contact oxide. Two different top electrode schemes are adopted and characterized in terms of Hall, sheet resistance, and optical transmittance measurements.

KEYWORDS: Nanowire, catalyst-free growth, solar cell, transparent contact, ITO, AZO
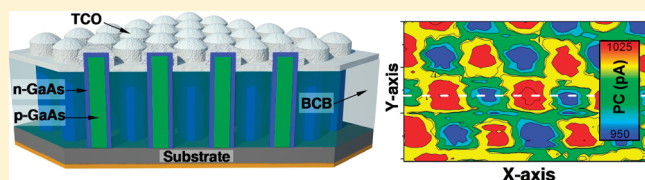
Nanostructured solar cells have gained much attention due to light trapping effects that drastically reduce the portion of reflected photons, therefore enhancing the optical absorption. Nanodomes,[1] nanocones,[2] nanoparticles,[3] and nanowires[4−9] (NWs) have the potential to improve performance compared to standard solar cells. The high surface-to-volume ratio increases the photoactive junction area and facilitates the carrier collection, enhancing the power conversion efficiency (PCE) with respect to bulk solar cells. In particular, compared to top-down[10] approaches, a bottom-up growth mode may lead to high-quality composition, crucial for any photovoltaic device. Furthermore, by exploiting radial junctions in each single NW, the light absorption (vertical direction) is decoupled from the carrier collection (radial direction), an unresolved issue in conventional planar solar cells.

Recently, silicon microwire solar cells[9] grown as ordered arrays have achieved PCE of 7.9%. However, due to the low optical absorption coefficient of silicon, long nanowires (∼60 μm) are required to absorb the above-band-gap photons. III−V, direct band gap technology requires ∼1 μm of material to efficiently absorb the photons and integration of radial multi-junctions becomes possible too. In addition, GaAs crystalline single junction solar cells[11] have recently demonstrated the highest PCE (up to 26.4%) in monojunction photovoltaics. Despite that, only one reported work regarding radial GaAs nanostructures,[12] based on Au-catalyzed vapor−liquid−solid (VLS) growth, demonstrates core−shell NW growth for photovoltaic applications. These photovoltaic devices exhibit low PCEs (0.83%), possibly due to the random distribution in terms of height, diameter, and position. Furthermore, the midgap trap states introduced by diffusion of Au catalyst into the NW[13]

degrade minority carrier lifetime and diffusion length on which photovoltaic devices rely. For successful devices, NW diameter, length, and filling ratio have to be carefully chosen and kept constant by the adoption of a regular geometry.[14] The less semi-conductor material required to absorb the same amount of photons with respect to thin films in conjunction with the possibility to peel off the NWs from the substrate and reuse it in subsequent growths, open up promising routes to low-cost, flexible solar cells. One approach to realizing a patterned architecture is to take advantage of lithography techniques to precisely define radius and center-to-center pitch in a mask from which the NWs can be grown. Such a mask translates into a uniform NW growth, allowing ease of processing/fabrication and avoiding adjacent NW junctions from contacting each other during growth. In addition, the small NW cross sections that can be realized allow the growth of junctions of dissimilar materials with high lattice-constant mismatch, permitting a prompt integration of heterogeneous material platforms.

Device structure and geometry, nonetheless, are not sufficient to ensure high-efficiency nanostructured photovoltaics: each interface must be carefully designed, including the nature of the contacts. This is especially true for degenerately doped semi-conducting oxides such as indium tin oxide (ITO) or aluminum zinc oxide (AZO). Their properties can profoundly modify carrier extraction/injection mechanisms once they come into contact with p-doped and n-doped semiconductors. This study discusses in detail the performance, in terms of electrical and
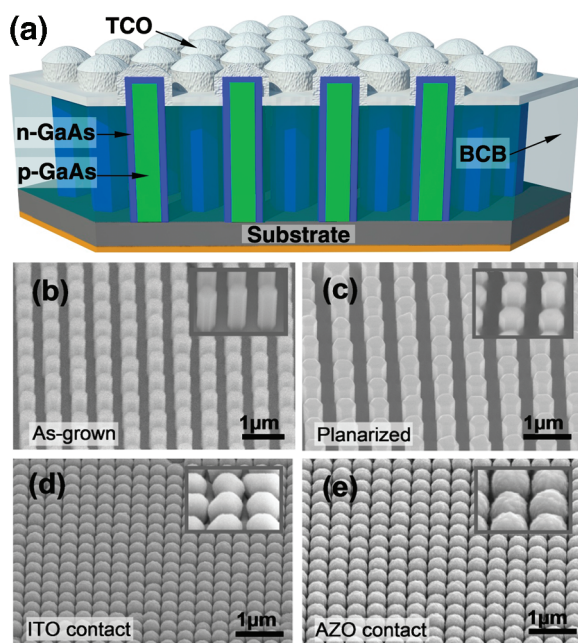
Figure 1. (a) Schematic drawing of the ordered GaAs NP solar cell. (b) 45°-tilt SEM image of an array of GaAs NPs with built-in radial p−n junctions. (c) 45°-tilt SEM image after BCB planarization and dry etch-back to expose only the NP tips. (d) 45°-tilt SEM image subsequent to ITO sputtering and relative coating of the NP tips. (e) 45°-tilt SEM image after AZO deposition on NP tips.

Figure 2. (a) Cross-sectional transmission electron microscope (TEM) image of a NP with ITO as top electrode and BCB as surrounding insulator. (b) Cross-sectional TEM image of a NP with AZO as top transparent contact.

electro-optical properties, of GaAs nanopillar (NP) solar cells based on a patterned periodic geometry. The devices are processed using with two transparent conducting oxides (TCO) to assess the most appropriate contact scheme.

The device schematic and fabrication scheme are shown in Figure 1. The core−shell NPs are formed by catalyst-free, selective-area metal−organic chemical vapor deposition. A 25 nm thick silicon dioxide mask is deposited by e-beam evaporation on a p$^+$-doped (111)B GaAs substrate and patterned using e-beam lithography and reactive-ion etching to have 500 μm × 500 μm arrays of holes with 600 nm spacing (0.25 mm^2 device area). The p-doped core is formed at a temperature of 685 °C for 15 min resulting in diameters of ∼200 nm and heights of ∼800 nm whereas the n-doped shell is grown at a reduced temperature of 665 °C for 2.5 min resulting in final diameters of 320 nm and heights of 900 nm. Disilane and diethyl zinc flow rates are chosen to produce carrier densities of $N_D = 1 \times 10^{18}$ cm^{-3} and $N_A = 3 \times 10^{17}$ cm^{-3}, calibrated on thin GaAs films. Figure 1a shows the schematic of the fabricated devices. Figure 1b illustrates a 45°-tilt scanning electron microscope (SEM) image of the as-grown NP array with built-in radial p−n junctions grown in situ. The hexagonal faceting suggests a good crystal growth quality. As aforementioned, the expected p-doped core diameter is ∼200 nm whereas the n-doped surrounding shell is estimated to be ∼60 nm wide. Due to the nanometer level dimensions, both highly doped core and shell are required in order to confine the depletion region well within the NW: a quasi-neutral core region is required in order for the carriers to travel all the way to the substrate and bottom electrode. Considering doping levels from planar calibrations, the total estimated depletion width in the NP amounts to ∼90 nm, ensuring quasi-neutral regions on both core and shell sides.
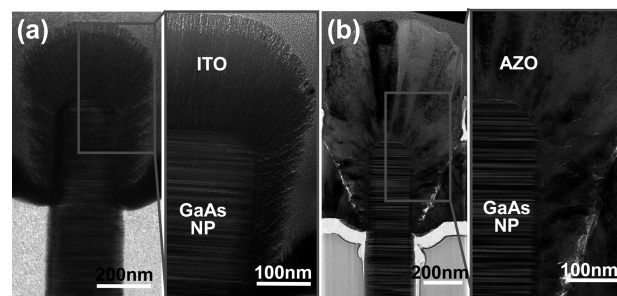
The device processing flow is initiated by a chemical treatment of the as-grown NP arrays in aqueous hydrochloric acid (HCl, 10% (v/v)) solution for 45 s to remove any native oxide on the surface followed by chemical passivation by means of ammonium sulfide $[(NH_4)_2S]$ solution (22% (v/v)) for 90 min to minimize the surface-state density.[15] Interface states, in fact, are likely to misbalance the electric fields and depletion regions at the nanometer scale, translating into poor or unpredicted behaviors in junction-based devices. After that, benzocyclobutene (BCB) resin (Cyclotene, Dow Chemical) is spun to completely cover the NP arrays in transparent electrical insulator. Subsequent to BCB hard-curing, the excess resin is removed by an O_2/CF_4 reactive ion etching to expose only the NP tips. Lastly, TCO (ITO (SnO_2/In_2O_3 10:90 wt %) or AZO (Al_2O_3/ZnO 2:98 wt %)) is deposited as top electrode. Bottom Ohmic contacts to the heavily doped substrate are formed by a Ti/Au (30 nm/200 nm) alloy.

As shown in Figure 1c, the exposure of the NP tips after plasma etching is 250 nm, leaving two-thirds of the nanostructures encapsulated in the BCB polymer. Subsequently, ITO or AZO are rf sputtered at room temperature at 200 W of applied rf power and 5 mT deposition pressure. These deposition parameters are found to be the optimum conditions for highly conductive and transmitting films. Figure 1d indicates that the deposition of ITO onto the NP array provides a conformal top contact across the NP tips. Figure 1e displays the SEM micrograph for the AZO sputtered contact on the device. AZO appears to have a more textured surface compared to ITO, suggesting a bigger average grain size. However, due to the final shape of the NP tips after deposition, light trapping is still expected due to the presence of gaps between adjacent NPs for both ITO and AZO.

The structural and morphological qualities of the TCOs are analyzed by cross-sectional transmission electron microscopy (TEM) images. Figure 2a shows a cross-sectional TEM image, sectioned by means of focused ion beam milling. The image reveals the ITO electrode in contact with a GaAs core−shell NP. The TCO is uniform in quality along the whole NP tip. Electron diffraction patterns taken during TEM (not included here) confirm the amorphous nature of the thin film. This is in agreement with previous works regarding ITO rf sputtered at room temperature: substrate temperatures[16] in excess of ∼200 °C are required to achieve a crystalline version of the material. The ITO thickness reduces at the bottom edges of the NP/BCB interface due to shadowing effects that decrease the deposition rate of ITO. However, the film remains continuous with a thinnest layer of around 60 nm. Figure 2b displays a cross-sectional TEM of
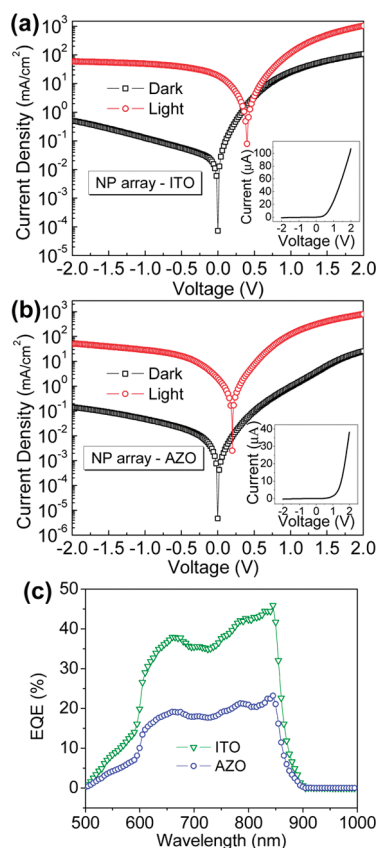
Figure 3. (a) Current density as a function of voltage (J–V) for the best NP solar cell with ITO as top contact both in the dark and under AM 1.5G illumination. The inset shows the I–V characteristic in linear scale for the device in the dark. (b) J–V characteristics of the best NP solar cell with AZO as top electrode both in the dark and under AM 1.5G illumination. The inset shows the I–V characteristic in linear scale for the device in the dark. (c) External quantum efficiency measurements of NP solar cells processed with ITO and AZO top contacts.

Table 1. Optoelectrical Characteristics of ITO and AZO

contact type	ITO	AZO
transmittance (%) (500 nm<λ<1000 nm)	>85	>85
sheet R (Ω/□)	15	627
doping concn (cm^{-3})	8.8×10^{20}	4.8×10^{19}
mobility (cm^2/(V s))	27	9
measured type	N	P

are indicative of well-behaving p–n junction in the NPs. This can be attributed to the regularity of the catalyst-free patterned growth (it eliminates parasitic shunting paths between adjacent NPs likely to occur in VLS-based arrays) and to the uniform BCB passivation/planarization layer. Under light, the device exhibits an open circuit voltage (V_{oc}) of 0.39 V, and a short circuit current (J_{sc}) of 17.6 mA/cm^2 with a fill factor (FF) of 37% resulting in a total PCE of 2.54%. Figure 3b presents J–V characteristics for a NP array with AZO as top electrode. Once again, the linear inset shows a good diode behavior of the junction in dark conditions with a rectification ratio of 183 (at ±1 V) and leakage currents of ~170 nA at −1 V. Upon illumination, the photovoltaic conversion results in a V_{oc} = 0.2 V, J_{sc} = 8.1 mA/cm^2, FF = 36% with a PCE = 0.58%. The planarization process is crucial in order to avoid undesired conduction between the top contact and the substrate that could reduce or annul the rectification action of the NPs. Furthermore, BCB has extensively been shown to additionally passivate GaAs devices, lessening the reverse leakage currents.[17−19] This also aids, for the ITO device, in enhanced V_{oc} (0.39 V) compared to 0.2 V previously reported in radial GaAs NW photovoltaics.[11]

The relatively low values of FF in both cases can be partly attributed to the presence of a non-negligible series resistance in the devices. Considering that the bottom electrodes are realized by well-established low-resistance alloys, the top electrodes (ITO and AZO) are causing a significant increase in the series resistance of the NP arrays, translating into low FF. From panels a and b of Figure 2 it can be noticed that the deposition of the oxides forms a thin layer at the interface NP tip/BCB, likely to cause a bottleneck in the conductivity of the overall top electrode. Furthermore, the sole ammonium sulfide passivation might not be sufficient to completely eliminate the surface states in the GaAs NWs and a SiNx shell as additional passivation could lead to higher efficiency. Also, the junction doping levels are estimated by means of planar growth tests; however dopant incorporation could be fairly different for the crystallographic directions involved in the NW. Figure 3c shows a comparison in terms of EQE measurements between ITO and AZO. This figure of merit quantifies the ratio of the number of charge carriers output by the array solar cell to the number of photons present in the AM 1.5 flux on the device. Although the shapes and trends are comparable over the spectrum of interest, the EQE measurement for the GaAs nanostructured solar cell processed with ITO as top electrode exhibits a more-than-doubled carrier collection in comparison with the AZO contact. Considering fairly similar work functions, the main cause for this unexpected behavior has to be sought in the difference of electrical and optical properties of the two conducting oxides.

Table 1 presents a comparison of the electro-optical properties of both ITO and AZO thin films on quartz substrate. The sputtering conditions are maintained exactly equal to the ones used for the top electrode depositions on the devices and carried
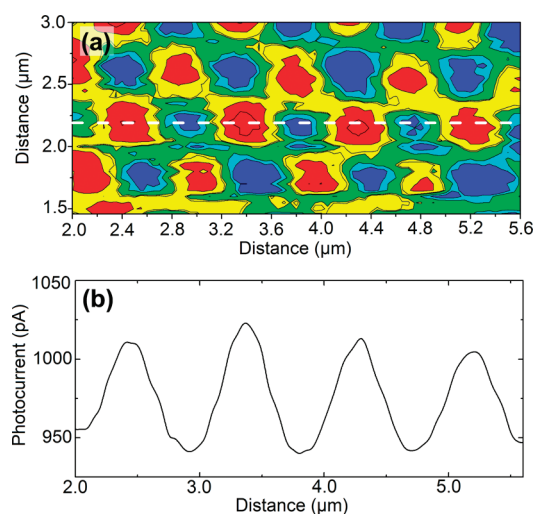
AZO contact deposited on top of the same NP structure. The AZO thin film appears thicker with respect to ITO due to the fact that the actual deposition rate on NPs is higher for the AZO target, even though the deposition conditions (sputtering power, substrate temperature, deposition time, pressure) are kept constant for both cases. Structurally, the AZO exhibits defects such as grain boundaries that can contribute to an increase in film resistivity. The conformation of AZO suggests a polycrystalline structure. This hypothesis is confirmed by electron diffraction patterns analyzed during TEM (not included here).

To characterize and compare the electrical properties of the devices based on these two different transparent top contacts, current density versus voltage (J–V) is measured both in dark conditions and under AM 1.5G normal illumination (1000 W/m^2, 1 sun) at room temperature. Also, external quantum efficiency (EQE) measurements are carried out to analyze the normalized distribution of the photocurrent along the visible spectrum of interest (from ~500 to 900 nm for GaAs). Figure 3a shows J–V characteristics both in the dark and under light. The inset illustrates, on a linear scale, the I–V of the sample with ITO as top contact: a high rectification ratio of 213 (at ±1 V) is achieved. Leakage currents in the order of ~236 nA at −1 V are measured. The values of rectification ratio and leakage currents

Figure 4. (a) Scanning photocurrent microscopy (SPCM) image of the best device processed with ITO as top transparent electrode. Red indicates largest photocurrent and blue the lowest. (b) Corresponding photocurrent line profile across the dashed line in panel a.

out on quartz in order to investigate only the thin film properties. The optical transmittance is obtained through Fourier transform infrared (FTIR) spectroscopy and calibrated with a bare quartz substrate as a baseline. The magnitudes of the transmittance are analogous, above 85% in the working optical range of the solar cells. This is in accordance with similar optical refractive indices as well as extinction coefficients for both transparent oxides.

The electrical analysis of the semiconducting oxides is characterized by means of four-point probe and Hall measurements. The sheet resistance for AZO is 627 $\Omega/\square$ with a measured thickness of 680 nm whereas the sheet resistance for ITO amounts to 15 $\Omega/\square$, for 630 nm thickness. This is in agreement with the trend observed in the $J-V$ device characteristics under dark (Figure 3a,b): the NP array processed with ITO exhibits a current of 107 μA at 2 V while the devices with AZO sputtered as top electrode show a current of 38 μA at 2 V. The Hall measurements are taken in a Van-der-Pauw geometry at room temperature under a nominal magnetic field of 2.5 T. The doping concentration and carrier mobility for the deposited ITO amount to 8.8×10^{20} cm^{-3} and 27 cm^2/(V s), respectively, with an n-type doping polarity. The same measurements for AZO reveal a doping concentration of 4.8×10^{19} cm^{-3} and a carrier mobility of 9 cm^2/(V s). The measured doping is p-type, in agreement with the presence of nitrogen during the sputtering process.[20] Consequently, ITO performs as a transparent anodic electrode whereas AZO functions as a transparent cathodic contact.

Considering one single NP as an elemental part of the device, the p-doped GaAs core is surrounded by the n-doped GaAs shell, constituting the photovoltaic junction. Under illumination, photogenerated minority carriers drift to their respective electrodes: electrons will travel along the n-doped shell whereas holes will be funneled into the p-doped core all the way to the substrate. Focusing on the top contacts, electrons will encounter a doping alignment of the type n/n$^+$ for n-doped shell/ITO while in the case of AZO electrons will go through an n/p$^+$ interface. For this reason, the extraction of the photogenerated carriers is greatly fostered when ITO is exploited as top electrode, translating into higher PCEs.

Finally, to verify that each NP is acting as a solar cell, high-resolution scanning photocurrent microcopy (SPCM) is used to image the array of NPs. SPCM is performed using diffraction-limited optics and a green HeNe laser ($\lambda = 544$ nm). Zero-bias photoconductivity is measured using a data acquisition board and preamplifier as the sample is scanned on a translational stage with 50 nm/step resolution in X and Y axes. The spot size of the beam is $\sim$300 nm as determined from full-width at $1/e^2$. The laser intensity for the measurements is attenuated to 103 μW/μm^2 to utilize the more sensitive settings of the preamplifier given the critical pitch of the NPs and the levels of photocurrent generated by the NP arrays. Figure 4a shows the SPCM map obtained for the best ITO device, with Figure 4b a line scan through the image. The map clearly shows alternating regions of higher and lower photocurrent forming a square array, with spacing of 600 nm between maxima. Note that because of the laser spot size and the close spacing between NWs, there is a nonzero photocurrent even when the laser beam is centered exactly between four NPs. The technique is able to resolve features smaller than the spot size[21] as the beam profile as well as location is of importance in generating the signal used in the microscopy. The current work is possibly the highest resolution display of the technique insofar as resolving dense features of known proximity. The SPCM mapping validates the fact that the collective $J-V$ characteristics of the array under light are indeed the superposition of all the photocurrent contributions coming from each individual NP. Furthermore, from the laser intensity and maximum generated photocurrent, an EQE of 2.8% is calculated. The small discrepancy between this number and the one obtained from the full illumination of the devices is mainly attributable to the fact that the laser light is fundamentally different from a monochromatically filtered source in regards to its relative full width at half-maximum.

In conclusion, this work presents the realization of a solar cell using a dense, uniform array of vertical core/shell NPs. Electrical characterization shows a device behavior affected by the doping type of the chosen transparent contact. EQE measurements quantify the difference in carrier extraction between AZO and ITO when used as top electrodes in GaAs NP photovoltaics. High-resolution SPCM characterization validates the independent functioning of each NW in the array with an individual peak photocurrent of $\sim$1 nA at 544 nm. Device efficiencies as large as 2.54% are obtained using ITO as the transparent conducting electrode. The absence of metal catalyst during growth translates into low-leakage-current devices. These results open a route to much higher efficiencies through the improvement of architecture as well as material and interface properties.

■ AUTHOR INFORMATION

Corresponding Author
*E-mail: giacomomariani@ucla.edu.

■ REFERENCES

(1) Zhu, J.; Hsu, C.; Yu, Z.; Fan, Z.; Cui, Y. *Nano Lett.* **2010**, *10*, 1979–1984.

(2) Zhu, J.; Yu, Z.; Burkhard, G. F.; Hsu, C.; Connor, S. T.; Xu, Y.; Wang, Q.; McGehee, M.; Fan, S.; Cui, Y. *Nano Lett.* **2009**, *9*, 279–282.

(3) Stupca, M.; Alsalhi, M.; Al Saud, T.; Almuhanna, A.; Nayfeh, M. H. *Appl. Phys. Lett.* **2007**, *91*, 063107.

(4) Fan, Z.; Razavi, H.; Do, J.; Moriwaki, A.; Ergen, O.; Chueh, Y.; Leu, P.; Ho, J.; Takahashi, T.; Reichertz, L.; Neale, S.; Yu, K.; Wu, M.; Ager, J.; Javey, A. *Nat. Mater.* **2009**, *8*, 648–653.

(5) Goto, H.; Nosaki, K.; Tomioka, K.; Hara, S.; Hiruma, K.; Motohisa, J.; Fukui, T. *Appl. Phys. Express* **2009**, *2*, 035004.

(6) Stelzner, T.; Pietsch, M.; Andra, G.; Falk, F.; Ose, E.; Christiansen, S. *Nanotechnology* **2008**, *19*, 295203.

(7) Hsueh, T.; Hsu, C.; Chang, S.; Guo, P.; Hsieh, J.; Chen, I. *Scr. Mater.* **2007**, *57*, 53–56.

(8) Dong, Y.; Tian, B.; Kempa, T.; Lieber, C. *Nano Lett.* **2009**, *9*, 2183–2187.

(9) Putnam, M.; Boettcher, S.; Kelzenberg, M.; Turner-Evans, D.; Spurgeon, J.; Warren, E.; Briggs, R.; Lewis, N.; Atwater, H. *Energy Environ. Sci.* **2010**, *3*, 1037–1041.

(10) Huang, J.; Chiam, S.; Tan, H.; Wang, S.; Chim, W. *Chem. Mater.* **2010**, *22*, 4111–4116.

(11) Green, M. A.; Emery, K.; Hishikawa, Y.; Warta, W. *Prog. Photovoltaics* **2010**, *18*, 346–352.

(12) Czaban, J. A.; Thompson, D. A.; LaPierre, R. R. *Nano Lett.* **2009**, *9*, 148–154.

(13) Jackson, J. B.; Kapoor, D.; Jun, S.; Miller, M. S. *J. Appl. Phys.* **2007**, *102*, 054310.

(14) Lin, C.; Povinelli, M. L. *Opt. Express* **2009**, *17*, 19371–19381.

(15) Cheng, C.; Chien, C.; Luo, G.; Chang, C.; Kei, C.; Yang, C.; Hsiao, C.; Perng, T.; Chang, C. *J. Phys.: Conf. Ser.* **2008**, *100*, 042002.

(16) Wakeham, S.; Thwaites, M.; Holton, B.; Tsakonas, C.; Cranton, W.; Koutsogeorgis, D.; Ranson, R. *Thin Solid Films* **2009**, *518*, 1355–1358.

(17) Sul, W. S.; Han, H. J.; Lee, H. S.; Lee, B. H.; Kim, S. D.; Rhee, J. K. *Mater. Res. Soc. Symp. Proc.* **2003**, *734*, 231–236.

(18) Chiu, H.; Yang, S. *IEEE Electron Device Lett.* **2002**, *23*, 243–245.

(19) Chiu, W.; Huang, F.; Wu, Y.; Lin, D.; Chan, Y.; Chen, S.; Chyi, J.; Shi, J. *Jpn. J. Appl. Phys.* **2005**, *44*, 2586–2587.

(20) Lu, H.; Lu, J.; Lai, C.; Wu, G. *Phys. B* **2009**, *404*, 4846–4849.

(21) Ahn, Y. H.; Tsen, A. W.; Kim, B.; Park, Y. W.; Park, J. *Nano Lett.* **2007**, *7*, 3320–3323.